



Contrasting changes in the sea surface temperature and upper ocean heat content in the South China Sea during recent decades

Fuan Xiao^{1,2} · Dongxiao Wang² · Lili Zeng² · Qin-Yan Liu² · Wen Zhou³

Received: 23 June 2018 / Accepted: 19 February 2019
© Springer-Verlag GmbH Germany, part of Springer Nature 2019

Abstract

Understanding the variability of upper ocean thermal conditions is key to regional climate prediction. In recent decades, the sea surface temperature and upper ocean heat content in the South China Sea (SCS SST and SCS OHC) have exhibited contrasting changes. In-situ observations and reanalysis data reveal a linear warming trend in SCS SST during 1975–2010 but a regime shift of SCS OHC during the late 1990s. Mixed layer heat budget analysis shows that the decreasing latent heat flux associated with a weakening surface wind contributes to SCS SST warming trend. The increasing SCS SST reflects a regional footprint of global warming. A simplified upper layer budget diagnosis reveals that more than half of OHC change results from the advection effect, which is caused by an anomalous SCS anticyclonic gyre associated with an anomalous negative wind stress curl. Then, the anomalous anticyclonic circulation deepens thermocline depth at the basin-scale, and result in the regime shift of SCS OHC. Changes in the ocean circulation are found to be related to the enhanced trade wind and a Matsuno-Gill response to cooling in the tropical central Pacific. Further analyses show that the regime shift process is attributed to a phase transition of the Interdecadal Pacific Oscillation (IPO) from positive to negative. Our results indicate that although the IPO is the sea surface low-frequency climate pattern, it could impact on the subsurface thermal variability in the SCS through the oceanic process.

Keywords Sea surface temperature · Upper ocean heat content · South China Sea · Regime shift · Interdecadal Pacific Oscillation

1 Introduction

Upper ocean thermal conditions have been shown to have a major impact on regional weather and climate systems, such as tropical cyclones and the monsoon (Price 1981; Pun et al. 2007; Feng and Hu 2014; Li et al. 2014; Huang et al. 2015). The South China Sea (SCS), the main pathway for water vapor and source of the East Asian summer monsoon, has properties characteristic of both the open ocean and a

regional ocean (Wang and LinHo 2002; Fang et al. 2003; Liu et al. 2004). Therefore, it is vital to study the characteristics and mechanisms behind anomalous upper ocean thermal conditions. Due to the unique location of the SCS, its upper ocean thermal conditions are quite different from those of the western Pacific Ocean and the Indian Ocean (Liu et al. 2004; Chiang et al. 2018). The variabilities of sea surface temperature (SST) and upper ocean heat content (OHC) in the SCS involve multiple time-scales, and are modulated by various external forcings (including the East Asian monsoon, the Kuroshio Current, the El Niño–Southern Oscillation (ENSO), and the Pacific Decadal Oscillation (PDO)) through atmospheric and oceanic processes.

On an interannual time-scale, the SCS upper ocean thermal conditions are strongly modulated by ENSO. Two major forcing pathways have been identified in previous studies. One is the “atmospheric bridge”, which reflects the air-sea exchange caused by local wind variation (Wang et al. 2000, 2002; Xie et al. 2003; Liu et al. 2004, 2014; Rong et al. 2007). The highest correlation between SCS SST and

✉ Lili Zeng
zenglili@scsio.ac.cn

¹ School of Geographical Sciences, Guangzhou University, Guangzhou 510006, China

² State Key Laboratory of Tropical Oceanography, South China Sea Institute of Oceanology, Chinese Academy of Sciences, Guangzhou 510301, China

³ Guy Carpenter Asia-Pacific Climate Impact Centre, School of Energy and Environment, City University of Hong Kong, Kowloon, Hong Kong SAR, China

ENSO was observed with a lag of 3–6 months (Klein et al. 1999). Further analysis revealed that an anomalous circulation (the “Western North Pacific anticyclone”) weakened the East Asian winter monsoon, the cloud cover and evaporation over the SCS then changed, and finally warmed SCS SST. The impact of ENSO on the SCS is not only confined to the SST, but also affects the subsurface ocean. He et al. (1997) analyzed 62,000 temperature-depth profiles and found that SCS OHC clearly increased during an El Niño year. Yan et al. (2010) further revealed that the westward propagation of negative (positive) OHC anomalies only occurred in the northern SCS during ENSO warm (cool) phases; this was mainly associated with the north–south difference of the wind field response to ENSO events. The atmospheric bridge can change the regional atmospheric circulation over the SCS, which induces both an anomalous surface heat flux and ocean circulation. So, this pathway can be considered the primary mechanism for the influence of external forcing on the SCS upper ocean thermal conditions. In addition to the atmospheric bridge, the “ocean channel” through the Luzon Strait is also an important forcing pathway to the SCS (Qu et al. 2004; Wang et al. 2006a, b; Tozuka et al. 2009; Yu and Qu 2013). This deep strait can transport the signal of ENSO into the SCS, with consequent changes in the regional ocean circulation and upper ocean thermal conditions. For example, the SCS throughflow (SCSTF) is considered as a conveyor belt transferring heat and freshwater between the SCS and the surrounding seas (Qu et al. 2006; Wang et al. 2006a, b; Fang et al. 2009). Liu et al. (2012) suggested that the SCSTF has significant negative correlation with the SCS OHC, which reflects the role of the SCSTF in cooling the upper ocean, and that this negative relationship is more significant during the El Niño mature phase.

Due to limited observational data, the characteristics and mechanisms of the upper ocean thermal conditions in the SCS over longer time-scales remained relatively unexplored. Thompson et al. (2017) removed the effect of the 1997/98 El Niño event, and indicated that the change in SCSTF was the main contributor to SCS SST regime shift in the late 1990s. In addition, Song et al. (2014) used expendable bathythermograph (XBT) data to study decadal variability of SCS OHC and suggested that advection (the net surface heat flux) was the main contributor to variability in SCS OHC before (after) 1980. However, neither Thompson et al. (2017) nor Song et al. (2014) discussed the mechanisms associated with large-scale climate factors. In addition, previous studies have always separately analyzed variabilities in SCS SST and SCS OHC, particularly on interannual time-scales (He et al. 1997; Klein et al. 1999; Qu et al. 2004; Wang et al. 2002, 2006; Yan et al. 2010). As we demonstrated in our earlier study, although SCS SST and SCS OHC were highly correlated (~ 0.53) during 1948–2010, distinct variations existed; for example, the extreme warm event of 2006/07 only occurred below the

surface (Xiao et al. 2018), which shows that variabilities in SST and OHC are inconsistent. The present study discusses the contrasting low-frequency variabilities of SCS SST and SCS OHC and focuses on their different trends and driving mechanisms associated with the large-scale climate factors.

The remainder of this paper is organized as follows. The data and statistical methods used in this study are introduced in Sect. 2. Section 3 details the observational evidence of different low-frequency variabilities of SCS SST and SCS OHC from 1975 to 2010 using in-situ and reanalysis datasets, and Sect. 4 investigates their associated mechanisms. Finally, a summary and discussion are given in Sect. 5.

2 Data and methods

2.1 Data

To track the contrast change in SCS SST and SCS OHC, monthly mean SST data from the Hadley Centre (HadISST; Rayner et al. 2003) and upper 300 m OHC estimated from Simple Ocean Data Assimilation (SODA, version 2.2.4) reanalysis data (Carton and Giese 2008) are analyzed. The Ishii dataset was compiled based on an analysis of different observational datasets (Ishii et al. 2006; Ishii and Kimoto 2009) and is used to verify the representativeness of the SODA temperature dataset. This study focuses on the time period of 1975–2010. To further verify the results of HadISST, SODA, and Ishii datasets, a newly updated physical oceanographic dataset known as the South China Sea Physical Oceanographic Dataset 2015 (hereafter, SCSPOD15, Zeng and Wang 2016; Zeng et al. 2016a, b) is also used. The SCSPOD15 assembles measurements from the World Ocean Database 2009 (WOD09), the Array for Real-time Geostrophic Oceanography (Argo) and South China Sea Institute of Oceanology (SCSIO) measurements.

To assess the cause of differences in SST and OHC changes in the SCS, ocean current data from SODA, net surface heat flux and its components, surface wind, and sea level pressure from the Twentieth Century Reanalysis (20CRv2) Project provided by the National Oceanic and Atmospheric Administration (NOAA) (Compo et al. 2008, 2011) are analyzed for the period 1975–2010. Sea surface height (SSH) was obtained from the French Archiving, Validation and Interpretation of Satellite Oceanographic data (AVISO) project during Jan 1993 and Dec 2010 (Ducet et al. 2000).

2.2 Methods

2.2.1 Statistical methods

Low-frequency anomalies for the reanalysis datasets are obtained from monthly data by the following steps: (1)

remove the seasonal cycle by subtracting the monthly climatology; (2) remove high-frequency components by applying a 7-year low-pass filter.

Empirical orthogonal function (EOF), composite difference, regression and correlation analyses are used in the present study. The statistical significance of the composite variables is estimated by Student's t test.

2.2.2 Regime shift index and Sverdrup relation

The regime shift detection algorithm developed by Rodionov (2004) is used to detect the specific time of climate regime shift. This regime shift index (RSI) identifies a regime shift or “significant change” when the difference between the two means exceeds a certain confidence level.

To understand the controlling factors and mechanisms behind the observed regime shift of OHC change, we utilize the Sverdrup relation to discuss ocean circulation changes in response to the large-scale wind stress curl. The equation is the same as that presented in Liu et al. (2001a):

$$\beta \frac{d\psi}{dx} = \text{curl} \left(\frac{\tau}{\rho_0} \right), \quad (1)$$

where $\beta = \frac{\partial f}{\partial y}$, f is the Coriolis parameter, y is the meridional coordinate, ψ is the stream function, x is the zonal coordinate, τ is the surface wind stress vector, and ρ_0 is the density for seawater (1027 kg m^{-3}). The Sverdrup transport in the interior SCS is evaluated by integrating Eq. (1) from east to west across the basin. The eastern boundary condition is $\psi = 0$, and the Luzon Strait is considered to be a closed boundary.

2.2.3 Mixed layer heat budget

To evaluate the contribution of net heat flux to the mixed layer temperature tendency, the mixed-layer heat budget is written (following Li et al. (2002)) as:

$$\frac{dT}{dt} = \frac{Q}{\rho C_p h_m} + ADV, \quad (2)$$

where h_m is the mixed layer depth, dT/dt is the mixed layer temperature tendency, $Q_{net} = Q/(\rho C_p h_m)$ is the net surface heat flux, the ADV is ocean advection. Here, ρ is the reference density of seawater (1027 kg m^{-3}), C_p is the specific heat capacity of seawater ($4007 \text{ J } ^\circ\text{C}^{-1} \text{ kg}^{-1}$), and h_m is defined as 45 m in our study region. All variables are processed to give a low-frequency anomaly prior to the calculation, as described in Sect. 2.2.1.

2.2.4 Upper layer heat budget

The heat budget for the upper 300 m OHC is written following Zhai and Sheldon (2012):

$$\underbrace{\int_{-h}^0 \frac{\partial}{\partial t} T dz}_{\text{OHC tendency}} = \underbrace{\frac{Q_{net}}{\rho C_p}}_{\text{heat flux}} - \underbrace{\int_{-h}^0 \nabla \cdot (\vec{V} T) dz}_{\text{advection}} \quad (3)$$

$$+ \underbrace{\int_{-h}^0 \kappa_h \nabla^2 T dz}_{\text{horizontal diffusivity}} + \underbrace{\frac{\partial}{\partial z} \int_{-h}^0 \kappa_v \frac{\partial T}{\partial z} dz}_{\text{vertical diffusivity}},$$

where T is ocean temperature, h is 300 m, Q_{net} is the net surface heat flux, \vec{V} is a three-dimensional velocity vector, and κ_h and κ_v are the horizontal and vertical diffusivities, respectively. Here, ρ is the reference density of seawater (1027 kg m^{-3}) and, c_p is the specific heat capacity of seawater ($4007 \text{ J } ^\circ\text{C}^{-1} \text{ kg}^{-1}$). The terms from the left-hand side of Eq. (3) correspond to terms for OHC tendency, heat flux, ocean advection, and horizontal and vertical diffusivities. However, when applying Eq. (3) to the SCS region on a low-frequency time-scale, some terms can be neglected and the equation can be simplified to capture the main factors; this is described in greater detail in Sect. 4.3.

3 Contrasting changes in SCS SST and SCS OHC

3.1 Low-frequency spatio-temporal modes

The EOF method is used to extract the dominant low-frequency spatio-temporal modes of SCS SST and SCS OHC anomalies. In the first EOF (EOF1) mode, the SCS SST is characterized by a warming trend over the entire basin, which accounts for 84.3% of the total variance (Fig. 1a). The region of significant SST variations has a northeast-southwest alignment, which is consistent with the direction of the East Asian monsoon (Fig. 1a). There is a region of rapid SST warming over the northeastern SCS, which agrees with the results of a previous study that revealed a regionally accelerated warming trend over the subtropical western boundary currents (Wu et al. 2012). In the second EOF (EOF2) mode, the SCS SST shows a north-south dipole with negative SST anomaly over the northern SCS and positive SST anomaly over the Gulf of Thailand, which only accounts for 5.8% of the total variance (Fig. 1b). In the time series, the corresponding principal component (PC1) of SST

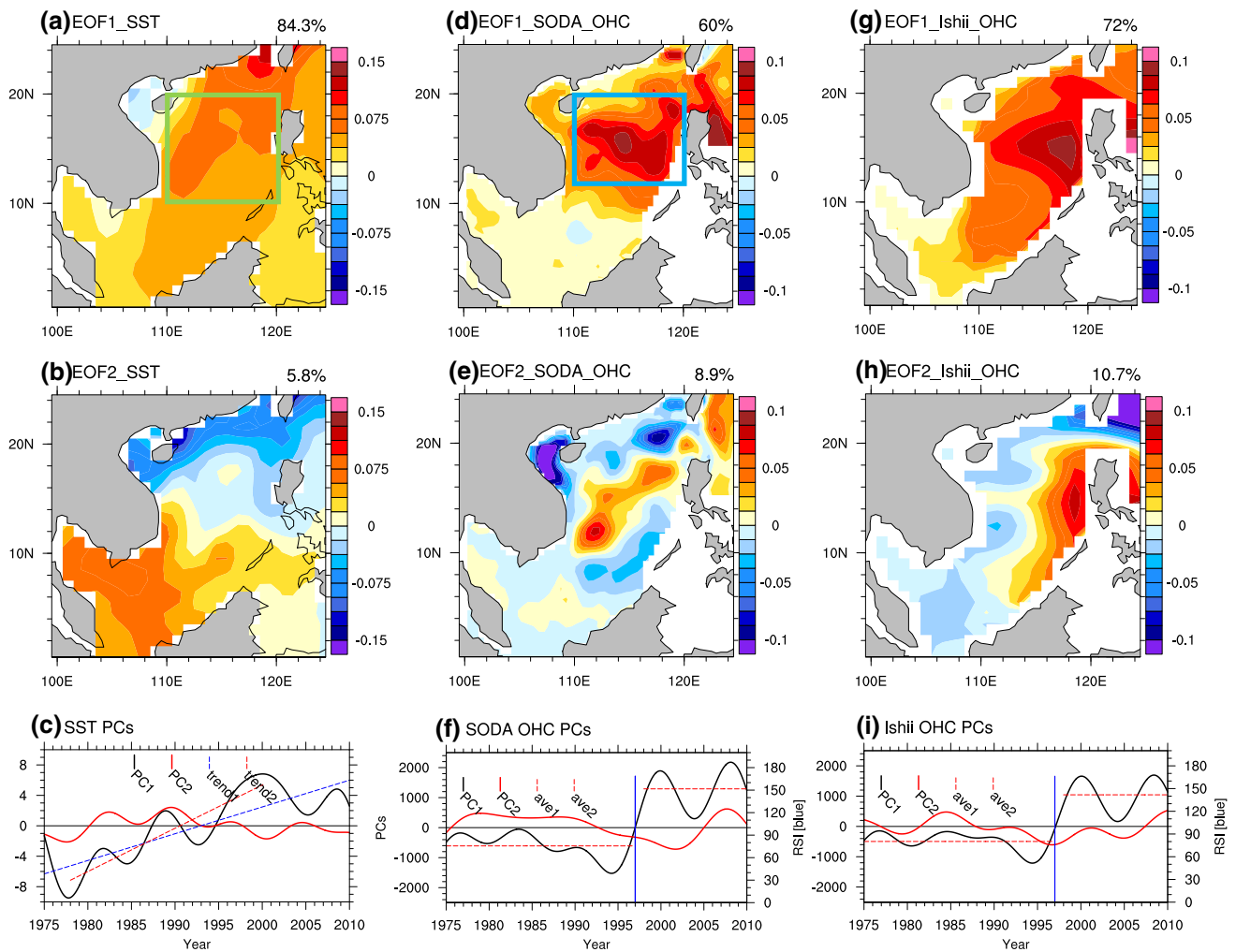


Fig. 1 **a** Spatial pattern of the first EOF mode (EOF1), **b** EOF2, and **c** corresponding principal component (PC1, black line; PC2, magenta line) for the low-frequency SST anomalies obtained from the Had-SSST data. **d–f** As in **a–c**, but for the upper 300 m OHC anomalies from SODA data. **g–i** As in **d–f**, but for Ishii data. Blue and red dashed lines in **c** indicate the linear trend for the periods 1975–2010 and 1978–1999, respectively. Blue lines in **f** and **i** represent the

Regime shift index (RSI) for PC1s which is significant at the 95% confidence level. Red lines in **f** and **i** represent the average values during 1975–1996 and 1998–2010, respectively. Green box indicates the region over the northern central SCS (10° – 20° N, 110° – 120° E) we calculate the averaged SST. Blue box in **d** indicates the region over the northern central SCS (12° – 20° N, 110° – 120° E) we calculate the averaged OHC

exhibits a linear warming trend, and the PC2 show no linear trend (Fig. 1c). The linear trend of PC1 for the periods 1978–1999 is larger than that of the period 1975–2010: for example, the mean low-frequency SST over the northern central SCS (10° – 20° N, 110° – 120° E) increased at a rate of $0.18^{\circ}\text{C}/\text{decade}$ during 1975–2010, while a faster warming rate of approximately $0.3^{\circ}\text{C}/\text{decade}$ occurred during 1978–1999. From the temporal and spatial distribution of EOF1 and EOF2, and by using North's test these two modes are distinguished from each other and are thus trusted to be stable (North et al. 1982).

The EOF1 pattern of the upper 300 m OHC estimated from SODA and Ishii data account for 60% and 72% of the total variance, respectively. The EOF1 spatial patterns of

the upper OHC based on the SODA and Ishii datasets both show a basin-wide positive anomaly mode, with the center located to the west of Luzon Island (Fig. 1d, g). Although there are different degrees of warming in the southern SCS, this does not influence the following discussions. PC1 is highly correlated between the SODA and the Ishii datasets and exhibits strong decadal variability (Fig. 1f, i). The RSI indicates that a significant regime shift likely occurred around 1997/98, which separates the time series into two subperiods: a cold period (1975–1996, hereafter P1) and a warm period (1998–2010, hereafter P2). We also give the results of EOF2 of the upper OHC based on the SODA and Ishii datasets (Fig. 1e, h). The results seem to have some differences between two datasets. For the SODA data, the

spatial pattern of the EOF2 has large amplitude oscillations in the deep basin and surrounding the deep basin. For the Ishii data, the spatial pattern of the EOF2 has large-amplitude oscillations in the eastern and western basin, and these oscillations are out of phase. The PC2 in the SODA and Ishii data show no significant trend or regime shift. The explained variances of the EOF1 modes in the SST and OHC are larger than 60%, so the EOF1 mode could represent the major characteristics of the SCS SST and SCS OHC on a low-frequency time-scale.

According to the above comparisons, it is evident that distinct differences exist between the dominant spatial modes of SCS SST and SCS OHC. The region of significant SST variations has a northeast-southwest alignment, which is consistent with the direction of the East Asian monsoon. However, the dominant region of OHC change is located in the northern central SCS: in particular, near the west of Luzon Island. The SST time series does not show a significant regime shift compared to that in the PC1 of the OHC, and instead present rather a linear warming trend. The EOF results for SCS SST and SCS OHC using the unfiltered monthly data show similar characteristics (figures not shown).

Both of the low-frequency variabilities in SCS SST and SCS OHC show increasing trend, to eliminate the influences of linear trend, we re-apply the EOFs after removing the linear trend (Fig. 2). The results show that when the linear trends are removed, the differences of PC1s between SST

and OHC are apparent. The regime shift appears to occur only in OHC and not in SST.

3.2 In-situ observational evidence

All available observations are selected over the main region (10° – 20° N, 110° – 120° E) from the SCSPD15, the location distribution is shown in Fig. 3a. We obtain the annual mean SCS SST anomaly and SCS OHC anomaly averaged over the main region (red solid lines in Fig. 3b, c). There are some remarkable discrepancies between the observational and reanalysis datasets, such as the variances of the observational results are larger than the grid data, but the linear warming trend of the SCS SST and the regime shift of the SCS OHC revealed by the HadISST and SODA datasets could be confirmed in the observations. Some other features could be also revealed by the observational and reanalysis datasets, for example, the SCS SST decreased after super El Niño year of 1997/98, but the SCS OHC retained in a positive anomaly period. The SCSPD15 dataset provides unprecedented observations in the SCS, there are still some gaps, and insufficient and uneven measurements in some years, just like in 1978 and 2003 in Fig. 3b, c (Zeng et al. 2016a, b). The non-uniform spatio-temporal distributions of SCSPD15 data prohibits their use in detecting associated driving mechanisms, and SODA reanalysis data are therefore used instead of the SCSPD15.

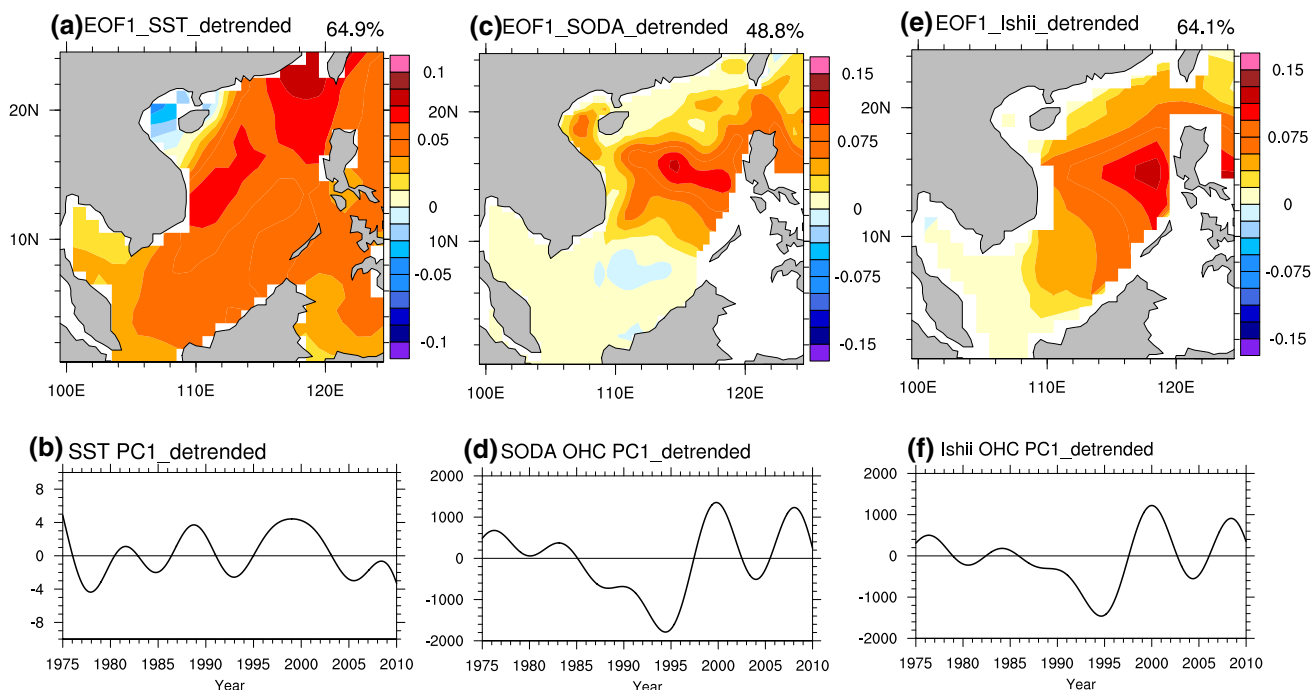


Fig. 2 **a** Spatial pattern of the EOF1, and **b** PC1 for the low-frequency SST anomalies obtained from the HadISST data after removing linear trend. **c**, **d** As in **a** and **b**, but for the upper 300 m OHC

anomalies from SODA data after removing linear trend. **e**, **f** As in **c** and **d**, but for Ishii data after removing linear trend

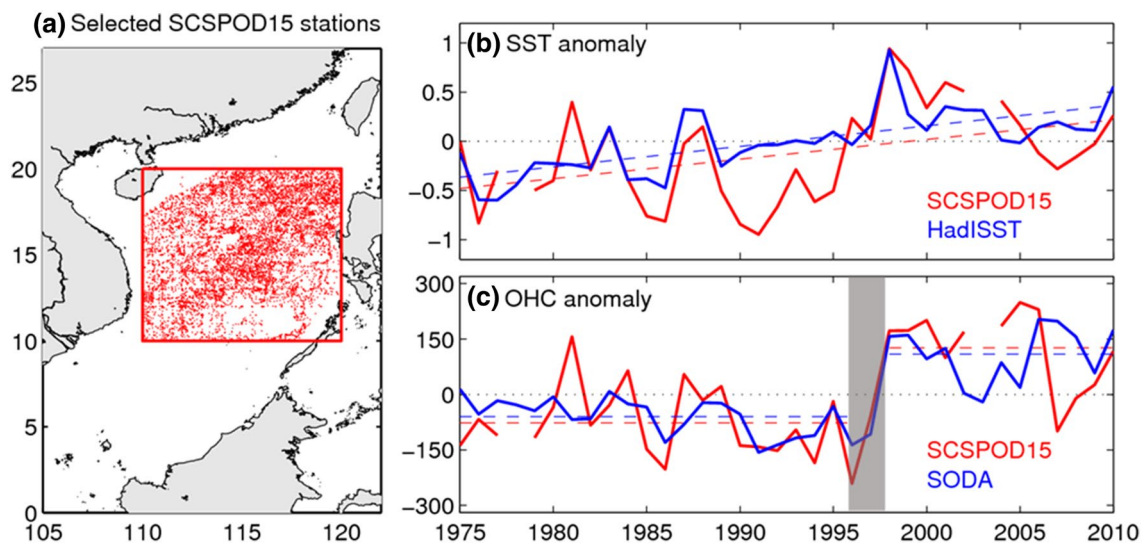


Fig. 3 **a** Locations of the SCSPD15 observation during 1975–2010 over the northern central SCS (10° – 20° N, 110° – 120° E). **b** Time series of the SST anomaly from HadISST (blue solid line) and SCSPD15 (red solid line) which are averaged over the northern central SCS (10° – 20° N, 110° – 120° E). Blue and red dashed lines indicate their corresponding linear trends. **c** Time series of the OHC anomaly

from SODA (blue solid line) and SCSPD15 (red solid line) which are averaged over the northern central SCS (12° – 20° N, 110° – 120° E). Blue and red dashed lines represent the average values during 1975–1996 and 1998–2010, respectively. Gray bar indicates 1997/98. The OHC anomaly from SODA is multiplied by 1.5 times for clarity

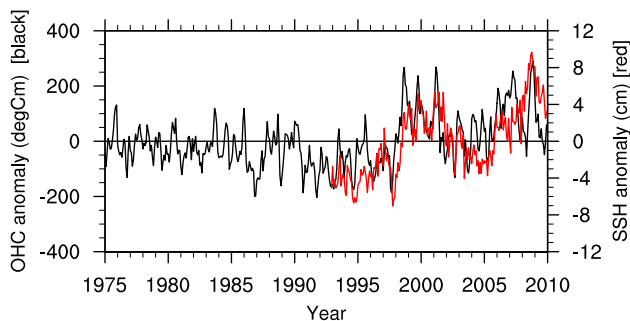


Fig. 4 Time series of OHC anomaly (black) from SODA reanalysis data and SSH anomaly (red) from AVISO averaged over the northern central SCS (blue box shown in Fig. 1d)

The previous study showed that SSH anomaly is a good indicator of the upper OHC anomaly (Fasullo and Gent 2017). Observations of SSH anomaly merged from several altimeter missions, allowing for near-global coverage, and starts in the late 1992. The results of the SSH anomaly which are averaged over the northern central SCS (12° – 20° N, 110° – 120° E) show a similar regime shift during 1997/98, and this agree well with the OHC anomaly (Fig. 4). The correlation coefficient between these two variables is about 0.65 during Oct 1992–Dec 2010, and on a low-frequency time-scale, the correlation coefficient reaches 0.9. So, all the evidences show that the contrasting changes in SCS SST and SCS OHC we revealed are robust.

4 Causes of contrasting changes in SCS SST and SCS OHC

4.1 Causes of linear SCS SST warming trend

To explore the different mechanisms involved in the low-frequency variabilities of SCS SST and SCS OHC, it is necessary to firstly understand the thermal structure of the upper 300 m. The monthly vertical profiles of upper 300 m temperature anomaly averaged over the northern central SCS (12° – 20° N, 110° – 120° E) are shown in Fig. 5, where Fig. 5a is the unfiltered result, and Fig. 5b is the result after a 7-year low-pass filter. It is evident the high-value center is concentrated below the mixed-layer from 50 to 150 m, and the amplitude of the mixed-layer temperature is less than that of the subsurface layer temperature. The decadal temperature variability in the subsurface is considerably more significant than that in the surface. Results show that the upper 300 m OHC is mainly dominated by the subsurface layer temperature anomaly in the SCS, this is consistent with our previous study (Xiao et al. 2018).

We firstly investigate the causes of the linear SCS SST warming trend. To answer this question, we compute the mixed-layer temperature tendency term and the net surface heat flux term averaged over the green box region in Fig. 1a following Li et al. (2002). As shown in Fig. 6a, the net surface heat flux is highly correlated with the mixed-layer temperature tendency ($R=0.6$, which exceeds 95% confidence level), which suggests that the heat flux is the

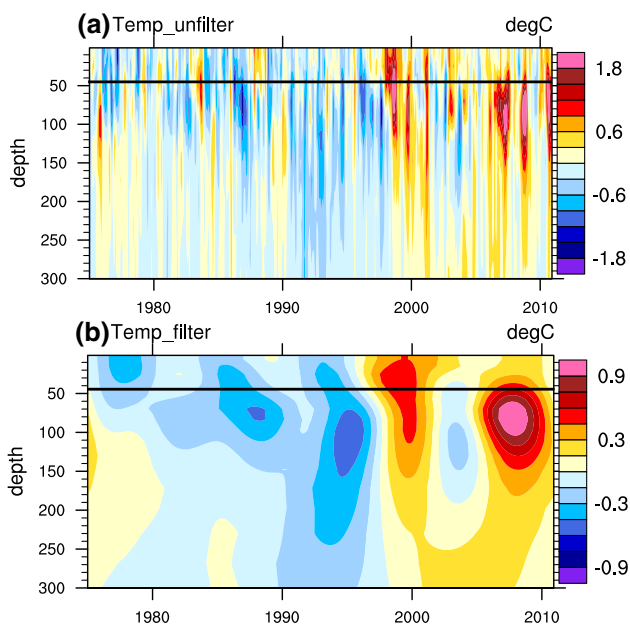


Fig. 5 **a** The monthly vertical profiles of upper 300 m unfiltered temperature anomaly obtained from SODA which are averaged over the northern central SCS (12°–20°N, 110°–120°E). **b** As in **a**, but for the 7-year low-pass filtered. Black line indicates the climatological mixed-layer depth (~45 m)

major contributor to low-frequency variability of SCS SST. Given the importance of net surface heat flux forcing, we further examine the relative contribution of its four components ($Q_{net} = LH + SH + SW + LW$), where the right-hand terms represent latent heat flux, sensible heat flux, shortwave radiation, and longwave radiation (Fig. 6b). Latent heat flux appears to be the major component of total net surface heat flux. Then, we give the linear trends of low-frequency SST

and surface winds in the SCS which are shown in Fig. 6c. The spatial distribution of the SST anomaly is similar to the EOF1 mode in Fig. 1a. The SCS is located in the East Asian monsoon region where the northeast monsoon (~9 m/s) prevails in winter and the southwest monsoon (~5 m/s) prevails in summer. The climatological wind direction in the SCS is the same as that of the northeast monsoon (Ding and Li 1999; Fig. 6d). A weakening trend in the prevailing surface winds is evident when observing the linear trend of low-frequency surface winds (Wang 2001; Yu et al. 2004, 2018; Wang et al. 2009; Zhu et al. 2012). Therefore, the decreasing latent heat flux associated with the weakening surface wind is the main reason for the SCS SST warming trend.

4.2 Causes of SCS OHC regime shift during late 1990s

In Sect. 4.1, we concluded that the decreasing latent heat flux associated with the weakening surface wind contributes to the SST warming trend. It is necessary to determine whether the net surface heat flux has an impact on OHC variability? We thus compute the OHC between 0 and 45 m and between 45 and 300 m, respectively, and then conduct an EOF analysis of the OHC tendency at these depths as HCT45 and HCT300, respectively. The results are shown in Fig. 7, where distinct spatial distributions can be observed for HCT45 and HCT300, which correspond to the difference between SCS SST and SCS OHC (Fig. 7a, b). The averaged SST tendency over 10°–20°N, 110°–120°E and OHC tendency over 12°–20°N, 110°–120°E are then computed to make a comparison with the PC1 of HCT45 and HCT300 (Fig. 7c, d). Results show correlation coefficients up to 0.86 and 0.72, respectively. Therefore, a correlation analysis is applied to determine the relationship between net surface

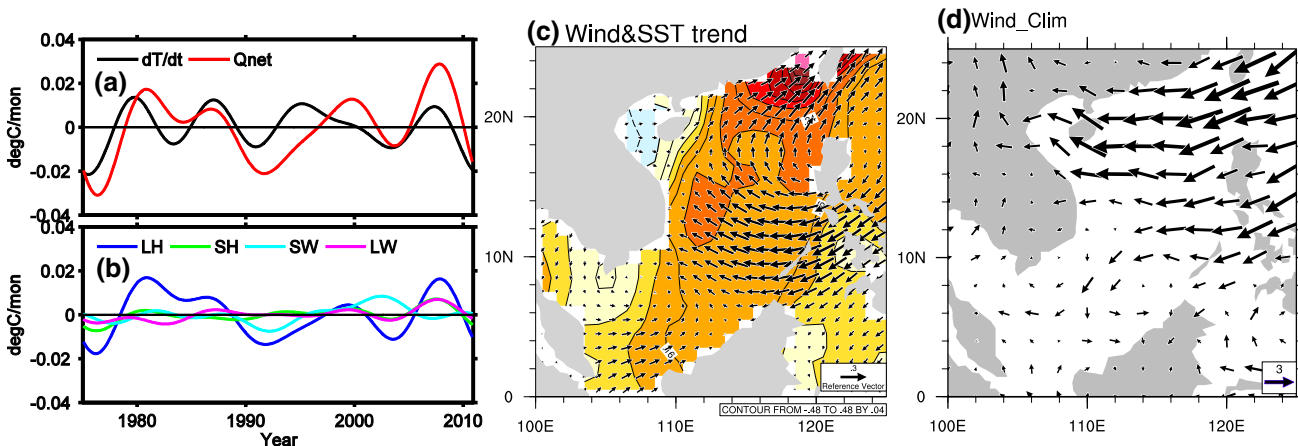


Fig. 6 Results of the mixed-layer heat budget averaged over the green box, **a** is the mixed-layer temperature tendency (black) and, the net surface heat flux term (red). **b** Four components of the net surface

heat flux. **a** Linear trends of the low-frequency SST (shading) and surface wind anomalies (vector) in the SCS during 1975–2010, **b** the climatological pattern of the surface wind fields

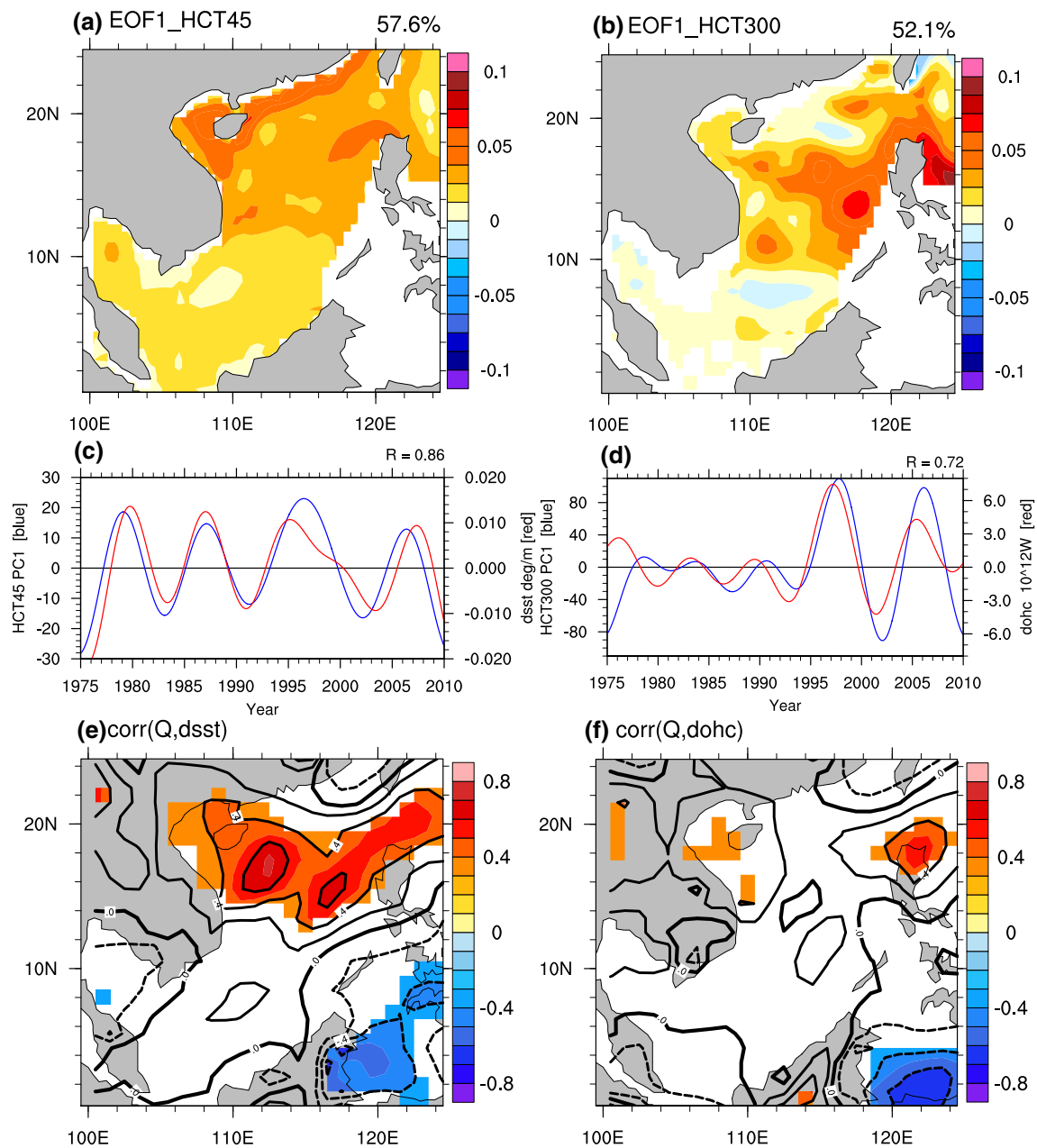


Fig. 7 Spatial pattern of the EOF1 for the low-frequency OHC tendency (HCT) between **a** 0–45 m and **b** 45–300 m obtained from the SODA reanalysis data. **c** The PC1 for the HCT between 0 and 45 m (blue) and the time series of the low-frequency SST tendency averaged over the northern central SCS (10°–20°N, 110°–120°E, red). **d** The PC1 for the HCT between 45 and 300 m (blue) and the HCT between 0 and 300 m averaged over the northern central SCS (12°–

20°N, 110°–120°E, red). The correlation coefficient between the low-frequency net surface heat flux and **e** the green box-averaged SST tendency in (red line in **c**) and **f** the blue box-averaged 300 m OHC tendency (red line in **d**). Shading area indicates the correlation coefficients exceed the 95% confidence level (*t* test) for the period 1975–2010

heat flux and SST tendency (Fig. 7e), and net surface heat flux and OHC tendency (Fig. 7f). Results show that the net surface heat flux is highly correlated with the SST tendency over the northern central SCS, which is consistent with our mixed-layer heat budget result. The lack of an obvious relationship between the OHC tendency and net surface heat

flux illustrates the net surface heat flux was not responsible for warming the subsurface water. We thus investigate this mechanism and the linkage between the regime shift of SCS OHC.

Figure 8a shows the change in upper OHC anomalies between P2 and P1 (1998–2010 minus 1975–1996) in SODA

reanalysis. The entire SCS was warmer during P2 than in P1, particularly in the northern central SCS. Note that this basin-wide warming is also a prominent feature in EOF1 (Fig. 1d). As discussed in the previous paragraph, the increasing OHC in the northern central SCS basin is less relevant to the net surface heat flux into the ocean (Fig. 7f). Previous studies have suggested that, on a low-frequency time-scale, changes in the ocean circulation and related heat transport are the major factors determining the upper OHC anomalies (Bjerknes 1964). The difference in the ocean currents averaged over the upper 300 m between these two time periods is shown in Fig. 8b. The changes in upper layer circulation display a significant anticyclonic gyre in the northern central SCS and a cyclonic gyre in the southern SCS, with an anomalous westward flow.

We then use the Sverdrup relation, Eq. (1), to estimate ocean circulation changes in response to changes in the local wind stress curl. The Luzon Strait is considered to be a closed boundary so that interior Sverdrup transport is caused only by the wind stress curl. Figure 8c shows the difference in interior Sverdrup transport between P2 and P1. Significant anomalous southward interior Sverdrup transport north of 12°N can be seen in Fig. 8c, with a maximum strength of about 0.7 Sv ($1 \text{ Sv} = 10^6 \text{ m}^{-3} \text{ s}^{-1}$) at 17°N. The anomalous Sverdrup transport is forced mainly by the local wind stress curl and is balanced by an anomalous western boundary current transport, which forms an anomalous anticyclonic circulation in accordance with the results in Fig. 8b.

Furthermore, we use the upper layer heat budget, Eq. (3), to conduct a heat budget analysis, with the aim of estimating the

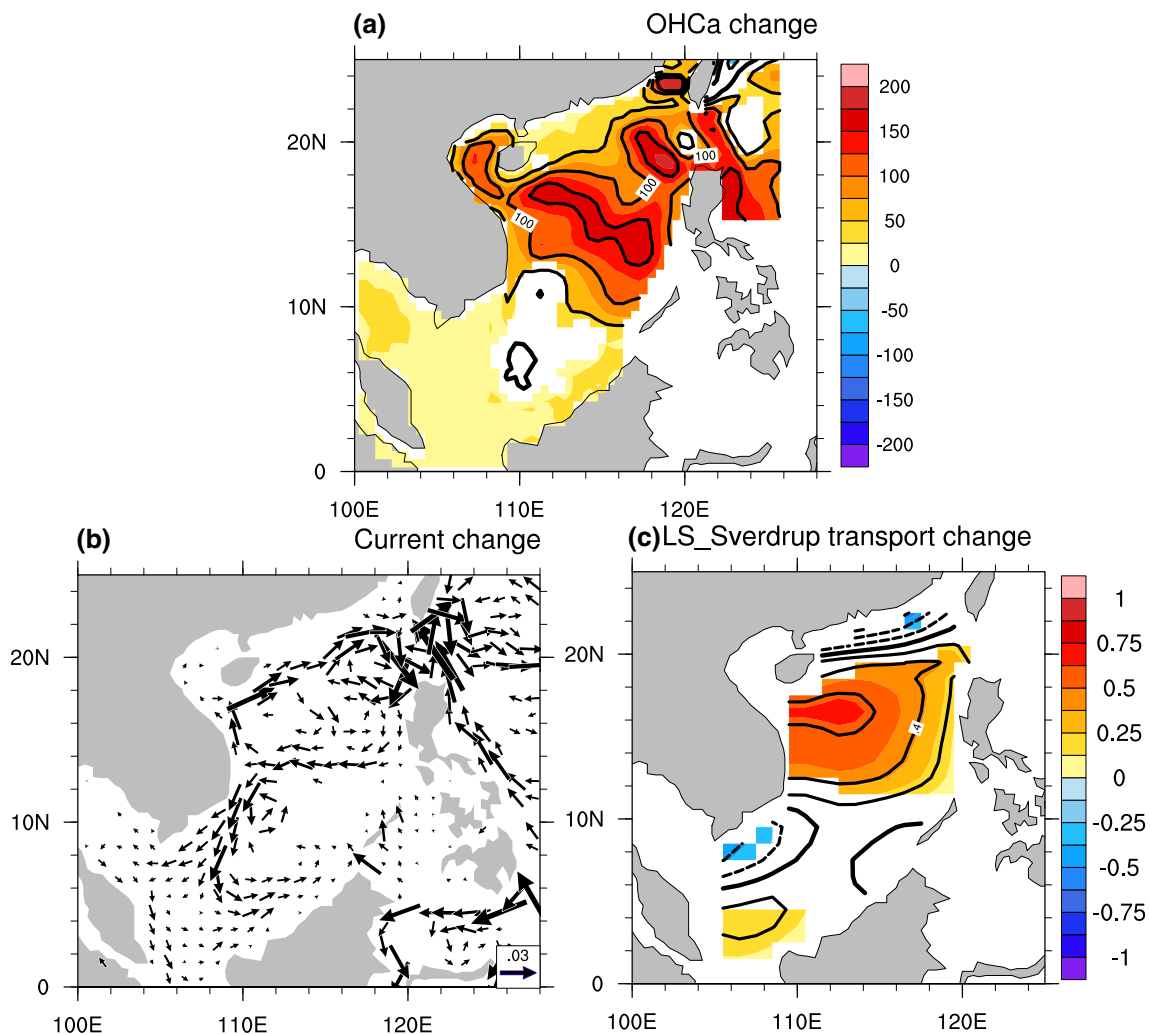


Fig. 8 Changes between two OHC periods (P2–P1, i.g., the 1998–2010 time period minus the 1975–1996 time period) for, **a** the upper 300 m OHC ($^{\circ}\text{C m}$), **b** ocean currents averaged over the upper 300 m (m s^{-1}), and **c** Sverdrup stream function ($\text{Sv} = 10^6 \text{ m}^3 \text{ s}^{-1}$) when the

Luzon Strait is taken as a closed boundary. Shaded areas and vectors are only shown for differences exceeding the 95% confidence level (t test)

relative contributions of the atmospheric and ocean circulation to the regime shift of OHC change.

4.3 Simplified upper heat budget

When applying the upper layer heat budget, Eq. (3), to the SCS region on a low-frequency time-scale, some terms may be neglected. First, the influence of anomalous Ekman transport/pumping and diffusion on OHC change is negligible in comparison with that of the geostrophic current in the SCS (Li et al. 1999; Qu 2000), so the Eq. (3) may be written as

$$\frac{\partial}{\partial t} \int_{-h}^0 T dz \approx \frac{Q_{net}}{\rho c_p} - \int_{-h}^0 \nabla \cdot (\vec{v}T) dz, \tag{4}$$

Furthermore, the anomalous advective transport is found to be due mostly to the advection of mean temperature by anomalous currents, rather than the transport of anomalous temperature by the mean flow in the western boundary current region (Qiu 2000; Eden and Jung 2001).

In Fig. 9, we show an example of the different components of the anomalous advective transport across 12°N in the SCS (the southern boundary of the control volume in the next discussion). The result confirms that the anomalous advective transport in the SCS is also determined by the advection of mean temperature by anomalous currents. Finally, the contribution of eddies to OHC change is neglected because it is difficult to estimate.

Integrating Eq. (4) over the control volume in the SCS (the upper 300 m between 12° and 20°N and between 110° and 120°E), we obtain

$$\frac{\partial}{\partial t} \int \rho c_p T dV \approx \int Q_{net} dS + \alpha \rho c_p \psi \Delta \bar{T}, \tag{5}$$

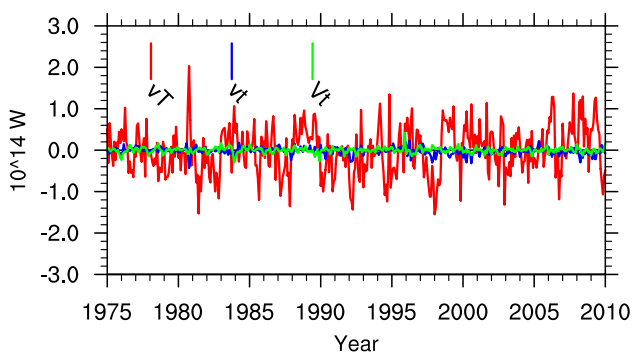


Fig. 9 The anomalous heat transport across 12°N and 110°–120°E. “vT” is the advection of mean temperature by anomalous currents, “vt” is the advection of anomalous temperature by anomalous currents, and “Vt” is the advection of anomalous temperature by mean currents

where S is the surface area of the control volume and $V = S \times h$ is the control volume. α is a nondimensional coefficient, that indicates the fractional change of the heat transport that takes place in the upper 300 m. According to Zhai and Sheldon (2012), if the response of ocean to wind stress is purely barotropic, $\alpha = \frac{300m}{depth}$ of the ocean which is roughly 0.15. If the baroclinic Rossby wave adjustment process is complete (Liu et al. 2001b; Bayler and Liu 2008; Cheng et al. 2016), $\alpha = 1$. But the situation is more complex, because the second term on the right-hand side of Eq. (5) includes the contributions of Kuroshio intrusion on the heat transport in the SCS. According to Xu and Oey (2015), the contribution of the Kuroshio intrusion to the SSH variability accounts for more than 30% in the northern SCS. So, on a low-frequency time-scale, we assume $\alpha = 0.5 - 0.7$. $\Delta \bar{T}$ is the temperature difference between the regions where the boundary currents enter and leave the control volume. In this study, $\Delta \bar{T} = \bar{T}_{12^{\circ}N, 110^{\circ}-120^{\circ}E} - \bar{T}_{20^{\circ}N, 110^{\circ}-120^{\circ}E}$, and varies with time. T , Q_{net} , and ψ are anomalies with respect to the climatology.

For P1 (1975–1996),

$$\frac{\partial}{\partial t} OHC = \frac{\partial}{\partial t} \int \rho c_p T dV \approx \int Q_{net} dS + \alpha \rho c_p \psi \Delta \bar{T}. \tag{6}$$

The time-integrated Eq. (5) becomes

$$OHC_1 = \int_{1975}^{1996} OHC \approx \int_{1975}^{1996} \int Q_{net} dS dt + \int_{1975}^{1996} \alpha \rho c_p \psi \Delta \bar{T} dt. \tag{7}$$

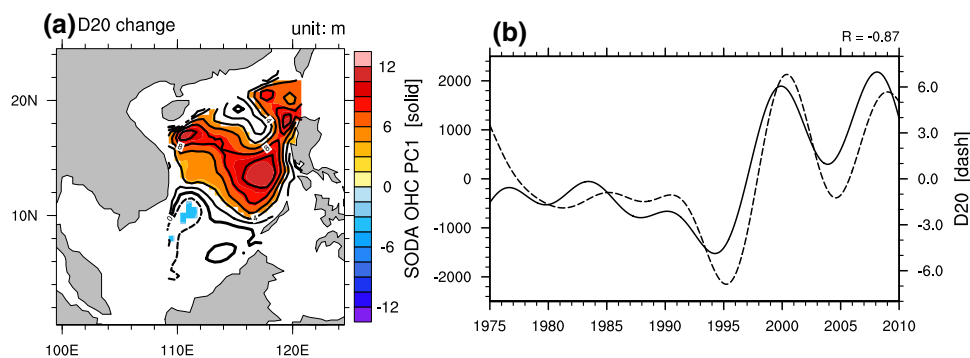
We can obtain the same equation for P2 (1998–2010),

$$OHC_2 = \int_{1998}^{2010} OHC \approx \int_{1998}^{2010} \int Q_{net} dS dt + \int_{1998}^{2010} \alpha \rho c_p \psi \Delta \bar{T} dt. \tag{8}$$

The accumulated OHC change between P2 and P1 ($OHC_2 - OHC_1$) is estimated to be 7.74×10^{22} J, and the time-integrated net surface heat flux anomaly difference is about 1.41×10^{21} J, which accounts for about 2% of the total OHC change. Assuming $\alpha = 0.5$, we estimate the difference in heat transport induced by the anomalous circulation between P2 and P1 as 4×10^{22} J, which accounts for about 51.7% of the total OHC change. If we assume $\alpha = 0.7$, the changes in anomalous heat transport between P2 and P1 is about 5.6×10^{22} J, which accounts for about 72.3% of the total OHC change.

We also note that the pattern of the Sverdrup transport change in Fig. 8c is similar with that of the OHC change in Fig. 8a. Previous discussions shown that the anomalous local wind stress curl forced an anomalous gyre-scale anti-cyclonic circulation in the SCS. Figure 10a shows the thermocline depth change between P2 and P1, in this study, the

Fig. 10 **a** As in Fig. 8a, but for the thermocline depth. **b** Time series of the low-frequency thermocline depth which are averaged over the northern central SCS (12°–20°N, 110°–120°E, dashed line) and PC1 for the OHC in the SODA data (solid line)



depth of the 20 °C isotherm (D20) is used as a proxy for the thermocline depth. The thermocline depth deepened in the northern central SCS significantly during P2 than P1, the maximum depth is approximately 11 m (Fig. 10a). The results of the thermocline depth which is averaged over the northern central SCS (12°–20°N, 110°–120°E) is highly correlated (~ 0.87) with the OHC PC1 in the SODA data. The result indicates that the anomalous anticyclonic circulation deepens thermocline depth at the basin-scale, which made the pattern the OHC change is similar with that of the Sverdrup transport change.

4.4 Influence of large-scale forcing

The changes in ocean circulation associated with the local wind stress curl is the most important factor contributing to the regime shift for SCS OHC between P2 and P1. To detect the influence of large-scale forcing on the regime shift of SCS OHC, we show the difference in SST anomalies between these two time periods in Fig. 11a. The SST is significantly warmer than normal in the northern Pacific Ocean, but cooler than normal in the tropical regions, especially in the tropical central and eastern Pacific. This pattern is a typical negative Interdecadal Pacific Oscillation (IPO) pattern (Power et al. 1999; Arblaster et al. 2002; Folland et al. 2002). Previous studies have shown that the IPO acts as a climate modulator in many parts of the globe (Folland and Salinger 1995; Salinger and Mullan 1999; Meehl and Hu 2006; Dai 2013). Significant modulation of the ocean circulation and SSH in the SCS by the IPO/PDO on an interdecadal timescale has also been reported (Yu and Qu 2013; Cheng et al. 2016). Corresponding to SST change, anomalously high sea level pressure (SLP) is centered at mid-latitudes and over the tropical eastern Pacific, and anomalously low SLP occurs in the western Pacific. Thus, the Pacific trade winds are enhanced during P2 compared with P1. The changes in SLP and wind are consistent with the change in sign of the IPO in the late 1990s (England et al. 2014). A significantly anomalous anticyclonic circulation covers the SCS (the red box in Fig. 11b) and the Philippine Sea. Matsuno (1966) and Gill (1980) showed that in response to an equatorial

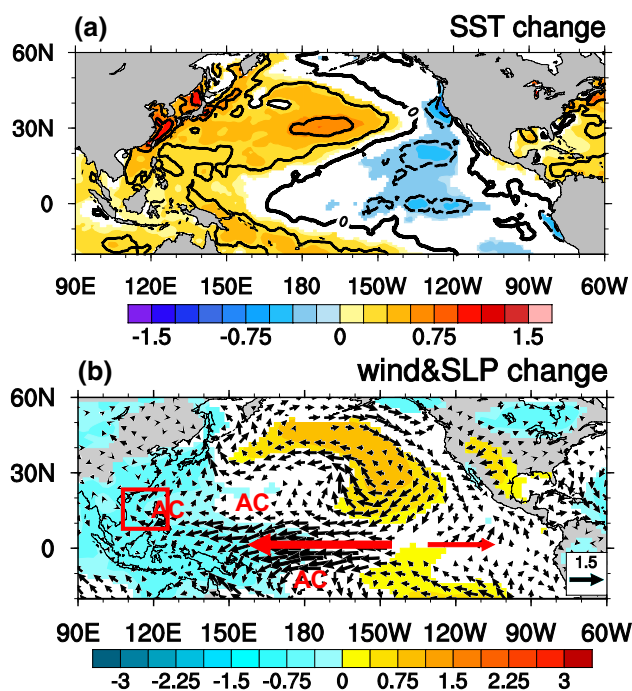
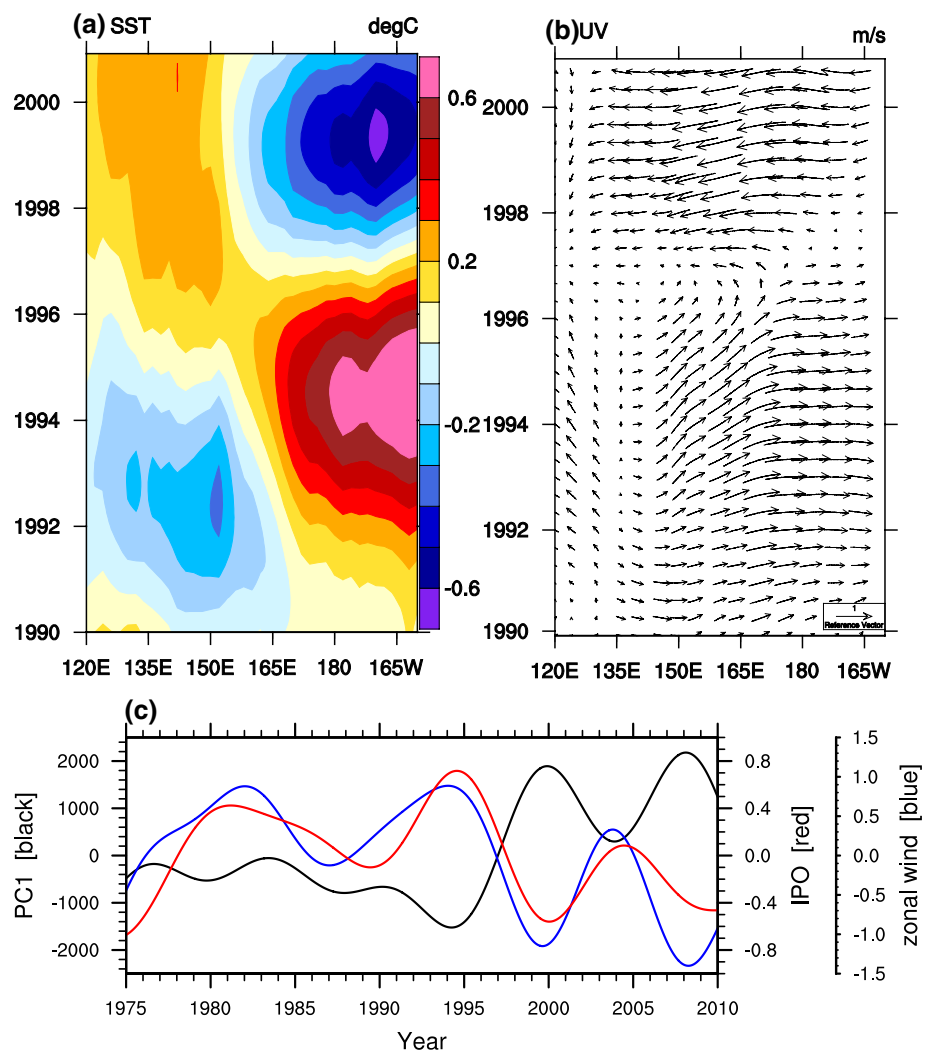


Fig. 11 Changes between two OHC periods (P2–P1, i.g., the 1998–2010 time period minus the 1975–1996 time period) for **a** SST (°C), **b** sea level pressure (shading: hPa) and surface wind (vectors: m s^{-1}). Only the differences exceeding the 95% confidence level (t test) are plotted. Red box in **b** is the SCS region. “AC” means anticyclone, red arrows are the wind directions

heat sink (source), twin anticyclones (cyclones) and easterlies (westerlies) with downward (upward) flow developed to the west of the heat sink (source). This is referred to as the Matsuno-Gill pattern. The patterns demonstrated in Fig. 11b are quite similar to a Matsuno-Gill response. When the IPO phase changes from positive to negative, the response of the surface wind is the enhanced trade wind and the anticyclonic wind anomalies over the SCS.

A Hovmöller diagram (averaged over 9.5°S–9.5°N) for SST shows that the IPO changed its phase from positive to negative around 1997 (Fig. 12a). Accordingly, an easterly equatorial trade wind anomaly then occurred in the Pacific (Fig. 12b). The IPO index (Henley et al. 2015) is used to

Fig. 12 Hovmöller diagram of the low-frequency **a** SST anomaly, **b** for the surface winds, averaged over 9.5°S–9.5°N. **c** The low-frequency IPO index (red), zonal wind (blue) averaged over 120°E–160°W, 9.5°S–9.5°N, and OHC PC1 (black) shown in Fig. 10b



assess the relationship between trade winds (averaged over 120°E–160°W, 9.5°S–9.5°N), the IPO, and the SCS OHC (Fig. 12c). The IPO index, equatorial trade winds in the Pacific, and the OHC PC1 in the SODA data are highly correlated.

These results indicate that the IPO phase transition and the corresponding wind stress curl forced a horizontal gyre in the SCS, which is the major contributor to the regime shift of SCS OHC.

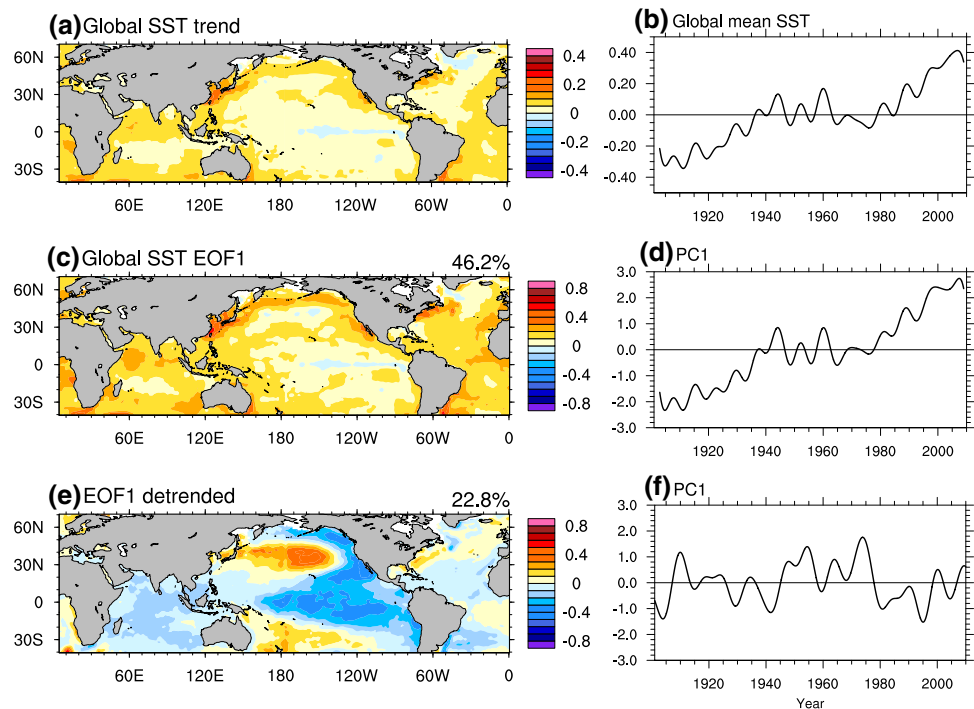
4.5 Footprint of global warming and IPO

A previous study discussed the mechanism involved in low-frequency SST variations over the China's coastal seas (Zhang et al. 2010). Results showed a correlation coefficient between the PC1 of low-frequency SST and global mean SST of 0.85, which reflects a regional footprint of global warming. Similar results were also found by Bao and Ren (2014). The spatial distribution of linear trend of the global SST on a low-frequency time-scale during 1901–2010

is shown in Fig. 13a, global mean SST anomaly shows an increasing trend, especially after 1970s (Fig. 13b). These results are also captured by the EOF1 results on a low-frequency time-scale (Fig. 13c, d). If we remove the linear trend of the SST on a low-frequency time-scale and re-apply the EOF analysis, the results of EOF1 shows an IPO pattern (Fig. 13e, f). The correlation coefficient between the PC1 of SCS SST and the PC1 of global SST is up to 0.92 (0.74, but after removing linear trend) during 1975–2010, which exceeds 95% confidence level, and the PC1 of SCS OHC is highly correlated with the PC1 of detrended global SST ($R = -0.65$, which exceeds 95% confidence level). From these results, the warming trend of the SCS SST and regime shift of the SCS OHC should be linked to global warming and the IPO, respectively.

We know that the SCS upper ocean thermal conditions are strongly modulated by ENSO on an interannual time-scale. The IPO is, an ENSO-like pattern of atmospheric and ocean climate variability and the second principal component of low-frequency global SST. It has a larger amplitude in the

Fig. 13 **a** The linear trend for the low-frequency SST anomaly obtained from the HadISST data, and **b** the global mean SST anomaly during 1901–2010. **c** Spatial pattern of the EOF1, and **d** corresponding PC1 for the low-frequency SST anomaly obtained from the HadISST data. **e, f** As in **c** and **d**, but after removing linear trend



central-west North Pacific, the eastern equatorial Pacific, and the central-west South Pacific. Therefore, upper ocean thermal conditions of the SCS should be controlled by the IPO on an interdecadal time-scale. However, the SCS SST time series shows no significant interdecadal variability associated with IPO, but a linear warming trend. Global warming is the first leading pattern of low-frequency global SST, and the WNP is one of most rapidly warming regions globally. It is very easy to understand that the SCS SST warming trend is related to global warming. Furthermore, we found the footprint of the IPO in the upper 300 m OHC (subsurface temperature) in this study. This result suggests that the subsurface temperature in the SCS may be less sensitive to net surface heat flux changes. The IPO phase transition and its associated local wind stress changes induced the thermocline depth acts as a modulator for the low-frequency variability of subsurface thermal conditions. This would illustrate that although the IPO is the sea surface low-frequency climate pattern, it could impact on the subsurface thermal variability in the SCS through the oceanic process.

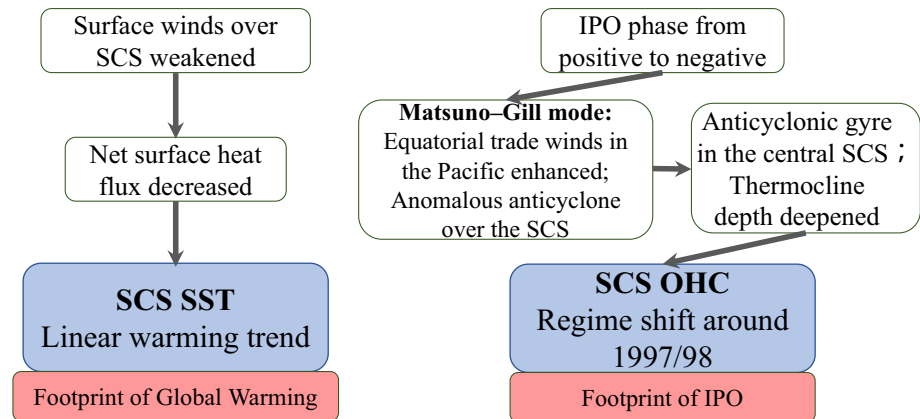
5 Conclusions and discussion

In this study, we have discussed the different behaviors of the low-frequency variabilities in SCS SST and SCS OHC by using observational and reanalysis data. The analysis reveals that SCS SST shows a linear warming trend during 1975–2010. Mixed layer heat budget analysis shows that the decreasing latent heat flux associated with weakening

surface wind is the main reason for SCS SST warming trend. Unlike the SCS SST, SCS OHC exhibited a significant regime shift during the late 1990s and the significant shift signal of the OHC was located mainly in the northern central SCS. A simplified upper layer heat budget equation was used to determine the contributions of atmosphere and ocean. In general, only about 2% of upper OHC change can be attributed to the increased net surface heat flux into the ocean. However, the main contributor to upper OHC change is the alteration in ocean circulation caused by the anomalous negative wind stress curl, the anomalous anti-cyclonic circulation then deepens thermocline depth at the basin-scale. Changes in the ocean circulation, are found to be related to the enhanced trade winds and a Matsuno-Gill response to cooling in the tropical central Pacific, and this is accompanied by an IPO phase transition from positive to negative. A schematic diagram summarizing these results is shown in Fig. 14.

The contribution of the Kuroshio intrusion to the ocean circulation cannot be neglected when we focus on the northern central SCS (Liu et al. 2001a; Xu and Oey 2015). In this study we neglect the contributions of the Kuroshio intrusion to the upper ocean heat transport because we want to capture the major contributor for the regime shift of SCS OHC. According Xiao et al. (2018), the Kuroshio intrusion transport seems to be shown a weakened trend, rather than a regime shift. Therefore, we supposed that the weakened Kuroshio intrusion may impact on the long-term increasing trend of the SCS OHC, rather than the regime shift process. How much the Kuroshio intrusion and meso-scale eddies

Fig. 14 Schematic diagram contrasting the low-frequency variability of SCS SST and SCS OHC, including their different behaviors and associated mechanisms



contribute to the upper ocean heat transport? We couldn't give a result quantitatively now, and the sensitivity experiment by using a coupled model may solve this problem, we are working on this.

Acknowledgements We thank two anonymous reviewers for their constructive comments. We thank Dr. Lijing Cheng (Institute of Atmospheric Physics, Chinese Academy of Sciences) and Dr. Wei Feng (Institute of Geodesy and Geophysics, Chinese Academy of Sciences) for their constructive suggestions. Numerous freely available data sets were used: SODA (<http://sodaserver.tamu.edu/assim/>); HadISST (<https://www.metoffice.gov.uk/hadobs/hadisst/>); AVISO (<https://www.aviso.altimetry.fr/en/data.html>); IPO index (<https://www.esrl.noaa.gov/psd/data/timeseries/IPOTPI/>). This work was supported by the National Natural Science Foundation of China under contract Nos. 41806027, 41776025, 41576012, 41606030, and the CAS/SAFEA International Partnership Program for Creative Research Teams.

References

- Arblaster JM, Meehl GA, Moore AM (2002) Interdecadal modulation of Australian rainfall. *Clim Dyn* 18(6):519–531
- Bao B, Ren G (2014) Climatological characteristics and long-term change of SST over the marginal seas of China. *Cont Shelf Res* 77:96–106
- Baylor EJ, Liu Z (2008) Basin-scale wind-forced dynamics of the seasonal southern South China Sea gyre. *J Geophys Res* 113:C07014. <https://doi.org/10.1029/2007JC004519>
- Bjerknes J (1964) Atlantic air–sea interactions. *Adv Geophys* 10:1–82
- Carton JA, Giese BS (2008) A reanalysis of ocean climate using simple ocean data assimilation (SODA). *Mon Weather Rev* 136:2999–3017
- Cheng X, Xie SP, Du Y, Wang J, Chen X, Wang J (2016) Interannual-to-decadal variability and trends of sea level in the South China Sea. *Clim Dyn* 46(9–10):3113–3126
- Chiang T, Hsin Y, Wu C (2018) Multidecadal changes of Upper-Ocean thermal conditions in the tropical northwest Pacific Ocean versus South China Sea during 1960–2015. *J Clim*. <https://doi.org/10.1175/JCLI-D-17-0394.1> (in press)
- Compo G et al (2008) The 20th century reanalysis project. In: Third WCRP International conference on reanalysis
- Compo G et al (2011) The twentieth century reanalysis project. *Q J R Meteorol Soc* 137:1–28
- Dai A (2013) The influence of the inter-decadal Pacific oscillation on US precipitation during 1923–2010. *Clim Dyn* 41(3–4):633–646
- Ding Y, Li C (1999) Onset and evolution of the South China Sea monsoon and its interaction with the ocean. China meteorological Press, Beijing (In Chinese)
- Ducet N, Le Traon PY, Reverdin G (2000) Global high-resolution mapping of ocean circulation from TOPEX/Poseidon and ERS-1 and-2. *J Geophys Res* 105(C8):19477. <https://doi.org/10.1029/2000JC900063>
- Eden C, Jung T (2001) North Atlantic interdecadal variability: Oceanic response to the North Atlantic Oscillation (1865–1997). *J Clim* 14:676–691
- England MH, McGregor S, Spence P, Meehl GA, Timmermann A, Cai W, Gupta AS, McPhaden MJ, Purich A, Santoso A (2014) Recent intensification of wind-driven circulation in the Pacific and the ongoing warming hiatus. *Nat Clim Change* 4:222–227
- Fang G, Wei Z, Choi BH, Wang K, Fang Y, Li W (2003) Interbasin freshwater, heat and salt transport through the boundaries of the East and South China Seas from a variable-grid global ocean circulation model. *Sci China Ser D* 46(2):149–161
- Fang G, Wang Y, Wei Z, Fang Y, Qiao F, Hu X (2009) Interocean circulation and heat and freshwater budgets of the South China Sea based on a numerical model. *Dyn Atmos Oceans* 47(1–3):55–72
- Fasullo JT, Gent PR (2017) On the relationship between regional ocean heat content and sea surface height. *J Clim* 30:9195–9211
- Feng J, Hu D (2014) How much does heat content of the western tropical Pacific Ocean modulate the South China Sea summer monsoon onset in the last four decades? *J Geophys Res Oceans* 119(7):4029–4044
- Folland CK, Salinger MJ (1995) Surface temperature trends and variations in New Zealand and the surrounding ocean, 1871–1993. *Int J Climatol* 15(11):1195–1218
- Folland CK, Renwick JA, Salinger MJ, Mullan AB (2002) Relative influences of the Interdecadal Pacific Oscillation and ENSO on the South Pacific Convergence Zone. *Geophys Res Lett* 29(13). <https://doi.org/10.1029/2001GL014201>
- Gill AE (1980) Some simple solutions for heat-induced tropical circulation. *Q J R Meteorol Soc* 106:447–462
- He Y, Guan C, Gan Z (1997) Interannual and interdecadal variations in heat content of the upper ocean of the South China Sea. *Adv Atmos Sci* 14:271–276
- Henley BJ, Gergis J, Karoly DJ, Power S, Kennedy J, Folland CK (2015) A tripole index for the interdecadal Pacific oscillation. *Clim Dyn* 45:3077–3090

- Huang P, Lin II, Chou C, Huang R (2015) Change in ocean subsurface environment to suppress tropical cyclone intensification under global warming. *Nat Commun* 6:7188
- Ishii M, Kimoto M (2009) Reevaluation of historical ocean heat content variations with time-varying XBT and MBT depth bias corrections. *J Oceanogr* 65:287–299
- Ishii M, Kimoto M, Sakamoto K, Iwasaka SI (2006) Steric sea level changes estimated from historical ocean subsurface temperature and salinity analyses. *J Oceanogr* 62:155–170
- Klein SA, Soden BJ, Lau NC (1999) Remote sea surface temperature variations during ENSO: evidence for a tropical atmospheric bridge. *J Clim* 12:917–932
- Li L, Wu R, Li Y, Gan Z (1999) A preliminary analysis of shallow water tidal aliasing in TOPEX/POSEIDON altimetric data. *Acta Oceanol Sinica* 21(3):7–14 (in Chinese with English abstract)
- Li T, Zhang Y, Lu E, Wang D (2002) Relative role of dynamic and thermodynamic processes in the development of the Indian Ocean dipole: an OGCM diagnosis. *Geophys Res Lett* 29(23):2110. <https://doi.org/10.1029/2002GL015789>
- Liu Q, Yang H, Liu Z (2001a) Seasonal features of the Sverdrup circulation in the South China Sea. *Prog Nat Sci* 11(3):202–206
- Liu Z, Yang H, Liu Q (2001b) Regional dynamics of seasonal variability in the South China Sea. *J Phys Oceanogr* 31:272–284
- Liu Q, Jiang X, Xie SP, Liu WT (2004) A gap in the Indo-Pacific warm pool over the South China Sea in boreal winter: seasonal development and interannual variability. *J Geophys Res* 109:C07012. <https://doi.org/10.1029/2003JC002179>
- Liu QY, Huang R, Wang D (2012) Implication of the South China Sea throughflow for the interannual variability of the regional upper-ocean heat content. *Adv Atmos Sci* 29:54–62
- Liu QY, Wang D, Wang X, Shu Y, Xie Q, Chen J (2014) Thermal variations in the South China Sea associated with eastern and central Pacific El Niño and their mechanisms. *J Geophys Res* 119:8955–8972
- Matsuno T (1966) Quasi-geostrophic motions in the equatorial area. *J Meteor Soc Japan* 44:25–43
- Meehl GA, Hu A (2006) Megadroughts in the Indian monsoon region and southwest North America and a mechanism for associated multidecadal Pacific sea surface temperature anomalies. *J Clim* 19:1605–1623
- North GR, Bell TL, Chalan RF (1982) Sampling errors in the estimation of empirical orthogonal functions. *Mon Wea Rev* 110:699–706
- Power S, Casey T, Folland C, Colman A, Mehta V (1999) Inter-decadal modulation of the impact of ENSO on Australia. *Clim Dyn* 15(5):319–324
- Price JF (1981) Upper ocean response to a hurricane. *J Phys Oceanogr* 11(2):153–175
- Pun IF, Lin II, Wu CR, Ko DS, Liu WT (2007) Validation and application of altimetry-derived upper ocean thermal structure in the western North Pacific Ocean for typhoon-intensity forecast. *IEEE T Geosci Remote* 45(6):1616–1630
- Qiu B (2000) Interannual variability of the Kuroshio extension system and its impact on the wintertime SST field. *J Phys Oceanogr* 30:1486–1502
- Qu T (2000) Upper-layer circulation in the South China Sea. *J Phys Oceanogr* 30:1450–1460
- Qu T, Kim YY, Yaremchuk M, Tozuka T, Ishida A, Yamagata T (2004) Can Luzon Strait transport play a role in conveying the impact of ENSO to the South China Sea? *J Clim* 17:3644–3657
- Qu T, Du Y, Sasaki H (2006) South China Sea throughflow: a heat and freshwater conveyor. *Geophys Res Lett* 33:L23617. <https://doi.org/10.1029/2006GL028350>
- Rayner NA, Parker DE, Horton EB, Folland CK, Alexander LV, Rowell DP, Kent EC, Kaplan A (2003) Global analyses of sea surface temperature, sea ice, and night marine air temperature since the late nineteenth century. *J Geophys Res* 108(D14):4407
- Rodionov SN (2004) A sequential algorithm for testing climate regime shifts. *Geophys Res Lett* 31:L09204. <https://doi.org/10.1029/2004GL019448>
- Rong Z, Liu Y, Zong H, Cheung Y (2007) Interannual sea level variability in the South China Sea and its response to ENSO. *Glob Planet Change* 55:257–272
- Salinger MJ, Mullan AB (1999) New Zealand climate: temperature and precipitation variations and their links with atmospheric circulation 1930–1994. *Int J Climatol* 19(10):1049–1071
- Song W, Lan J, Liu Q, Sui D, Zeng L, Wang D (2014) Decadal variability of heat content in the South China Sea inferred from observation data and an ocean data assimilation product. *Ocean Sci* 10:135–139. <https://doi.org/10.5194/os-10-135-2014>
- Thompson B, Tkalech P, Rizzoli PM (2017) Regime shift of the South China sea SST in the late 1990s. *Clim Dyn* 48(5–6):1873–1882
- Tozuka T, Qu T, Masumoto Y, Yamagata T (2009) Impacts of the South China Sea throughflow on seasonal and interannual variations of the Indonesian throughflow. *Dyn Atmos Oceans* 47:73–85
- Wang H (2001) The weakening of the Asian monsoon circulation after the end of 1970's. *Adv Atmos Sci* 18(3):376–386
- Wang B, LinHo (2002) Rainy season of the Asian–Pacific summer monsoon. *J Clim* 15:386–398
- Wang B, Wu R, Fu X (2000) Pacific–East Asian teleconnection: how does ENSO affect East Asian climate? *J Clim* 13:1517–1536
- Wang D, Xie Q, Du Y, Wang W, Chen J (2002) The 1997–1998 warm event in the South China Sea. *Chin Sci Bull* 47:1221–1227
- Wang D, Liu Q, Huang R, Du Y, Qu T (2006a) Interannual variability of the South China Sea throughflow inferred from wind data and an ocean data assimilation product. *Geophys Res Lett* 33:L14605. <https://doi.org/10.1029/2006GL026316>
- Wang G, Chen D, Su J (2006b) Generation and life cycle of the dipole in the South China Sea summer circulation. *J Geophys Res* 111:C06002. <https://doi.org/10.1029/2005JC003314>
- Wang L, Huang R, Gu L, Chen W, Kang L (2009) Interdecadal variations of the East Asian Winter monsoon and their association with quasi-stationary planetary wave activity. *J Clim* 22:4860–4872
- Wu L, Cai W, Zhang L, Nakamura H, Timmermann A, Joyce T, McPhaden MJ, Alexander M, Qiu B, Visbeck M, Chang P, Giese B (2012) Enhanced warming over the global subtropical western boundary currents. *Nat Clim Change* 2:161–166
- Xiao F, Zeng L, Liu QY, Zhou W, Wang D (2018) Extreme subsurface warm events in the South China Sea during 1998/99 and 2006/07: observations and mechanisms. *Clim Dyn* 50(1–2):115–128. <https://doi.org/10.1007/s00382-017-3588-y>
- Xie SP, Xie Q, Wang D, Liu WT (2003) Summer upwelling in the South China Sea and its role in regional climate variations. *J Geophys Res* 108:C8, 3261. <https://doi.org/10.1029/2003JC001867>
- Xu F, Oey L (2015) Seasonal SSH variability of the northern South China Sea. *J Phys Oceanogr* 45:1595–1609
- Yan Y, Qi Y, Zhou W (2010) Interannual heat content variability in the South China Sea and its response to ENSO. *Dyn Atmos Ocean* 50:400–414
- Yu K, Qu T (2013) Imprint of the Pacific decadal oscillation on the South China sea throughflow variability. *J Clim* 26:9797–9805
- Yu R, Wang B, Zhou T (2004) Tropospheric cooling and summer monsoon weakening trend over East Asia. *Geophys Res Lett* 31:L22212. <https://doi.org/10.1029/2004GL021270>
- Yu M, Li J, Zheng F, Wang X, Zheng J (2018) Simulating the IPOD, East Asian summer monsoon, and their relationships in CMIP5. *Theor Appl Clim*. <https://doi.org/10.1007/s00704-018-2442-4>
- Zeng L, Wang D (2016) Seasonal variations in the barrier layer in the South China Sea: characteristics, mechanisms and impact of warming. *Clim Dyn* 48(5–6):1911–1930

- Zeng L, Wang D, Chen J, Wang W, Chen R (2016a) SCSPOD14, a South China Sea physical oceanographic dataset derived from in situ measurements during 1919–2014. *Sci Data* 3:160029
- Zeng L, Wang D, Xiu P, Shu Y, Wang Q, Chen J (2016b) Decadal variation and trends in subsurface salinity from 1960 to 2012 in the northern South China Sea. *Geophys Res Lett* 43:12181–12189
- Zhai XM, Sheldon L (2012) On the North Atlantic Ocean heat content change between 1955–70 and 1980–95. *J Clim* 25:3619–3628
- Zhang L, Wu L, Lin X, Wu D (2010) Modes and mechanisms of sea surface temperature low-frequency variations over the coastal China seas. *J Geophys Res* 115:C08031. <https://doi.org/10.1029/2009JC006025>
- Zhu J, Liao H, Li J (2012) Increases in aerosol concentrations over eastern China due to the decadal-scale weakening of the East Asian summer monsoon. *Geophys Res Lett* 39:L09809. <https://doi.org/10.1029/2012GL051428>

Publisher's Note Springer Nature remains neutral with regard to jurisdictional claims in published maps and institutional affiliations.